Ultrasonics - Sonochemistry 54 (2019) 171–182

Contents lists available at ScienceDirect

Ultrasonics - Sonochemistry

journal homepage: www.elsevier.com/locate/ultson

Numerical modelling of acoustic streaming during the ultrasonic melt treatment of direct-chill (DC) casting

G.S. Bruno Lebon[a,e,*], Georges Salloum-Abou-Jaoude[a,b], Dmitry Eskin[a,f], Iakovos Tzanakis[c,d], Koulis Pericleous[e], Philippe Jarry[b]

[a] Brunel Centre for Advanced Solidification Technology (BCAST), Brunel University London, Uxbridge UB8 3PH, United Kingdom
[b] Constellium, Parc Economique Centr'alp, CS10027, Voreppe 38341 cedex, France
[c] Faculty of Technology, Design and Environment, Oxford Brookes University, Oxford OX33 1HX, United Kingdom
[d] Department of Materials, University of Oxford, Oxford OX1 3PH, United Kingdom
[e] Computational Science and Engineering Group (CSEG), Department of Mathematical Sciences, University of Greenwich, London SE10 9LS, United Kingdom
[f] Tomsk State University, Tomsk 634050, Russia

ARTICLE INFO

Keywords:
Acoustic cavitation
Liquid aluminium
Direct-chill casting
Numerical modelling
Ultrasonic melt processing
Non-linear acoustics

ABSTRACT

Acoustic streaming and its attendant effects in the sump of a direct-chill (DC) casting process are successfully predicted under ultrasonic treatment for the first time. The proposed numerical model couples acoustic cavitation, fluid flow, heat and species transfer, and solidification to predict the flow pattern, acoustic pressure, and temperature fields in the sump. The model is numerically stable with time steps of the order of 0.01 s and therefore computationally attractive for optimization studies necessitating simulation times of the order of a minute. The sump profile is altered by acoustic streaming, with the slurry region depressed along the centreline of the billet by a strong central jet. The temperature gradient in the transition zone is increased, potentially interfering with grain refinement. The cooling rate in the sump is also altered, thereby modifying the dendrite arm spacing of the as-cast billet. The relative position of the sonotrode affects the sump profile, with the sump depth decreased by around 5 mm when the sonotrode is moved above the graphite ring level by 100 mm. The acoustic streaming jet penetrates into the slurry zone and, as a result, the growth direction of dendritic grains in the off-centre position is altered.

1. Introduction

Ultrasonic melt treatment is applied to direct-chill (DC) casting for degassing, reducing the macrosegregation level, and refining the grain structure. Ultrasonic processing is performed by dipping one or several sonotrodes into the sump of the billet, as shown in Fig. 1. Eskin and Eskin attributed the grain refining effect of ultrasound to the activation of substrates by wetting, deagglomeration and dispersion of nucleating particles, and dendrite fragmentation, all associated with acoustic cavitation [1].

Numerical modelling of conventional DC casting is popular in the literature. DC casting models can be broadly classified as multiphase and continuum models. In multiphase models, the interfaces between the different phases are explicitly tracked. Ni and Beckermann [2] described a two-phase model based on volume averaging that enables the coupling between microscopic and macroscopic phenomena, but this approach is computationally expensive for optimization purposes. Bennon and Incropera [3] avoided the requirement of tracking phase interfaces by adopting a continuum formulation that integrates the microscopic description of transport behaviour. Their work has been clarified by Prescott et al. [4] who re-derived the continuum momentum equation and established the need for accurate closure rules to the continuum model. Vreeman et al. [5] later incorporated the transport of free floating dendrites in the slurry to this continuum model and modelled macrosegregation in DC casting. In a separate paper, Vreeman et al. [6] obtained a good comparison between empirical temperature and sump profiles with their continuum model: this approach is the starting point of our Computational Fluid Dynamics (CFD) model. Due to the low casting speeds and slow flows due to natural convection, the flow models in the sump are all laminar.

Mean-field models that closely couple solidification growth at the microscopic level and the macroscopic multiphase flow have been recently developed, both in DC casting and other processes such as vacuum arc re-melting [7]. Heyvaert et al. [8] adopted a three-phase

* Corresponding author at: Brunel Centre for Advanced Solidification Technology (BCAST), Brunel University London, Uxbridge UB8 3PH, United Kingdom.
E-mail address: Bruno.Lebon@brunel.ac.uk (G.S.B. Lebon).

https://doi.org/10.1016/j.ultsonch.2019.02.002
Received 14 November 2018; Received in revised form 31 January 2019; Accepted 1 February 2019
Available online 02 February 2019

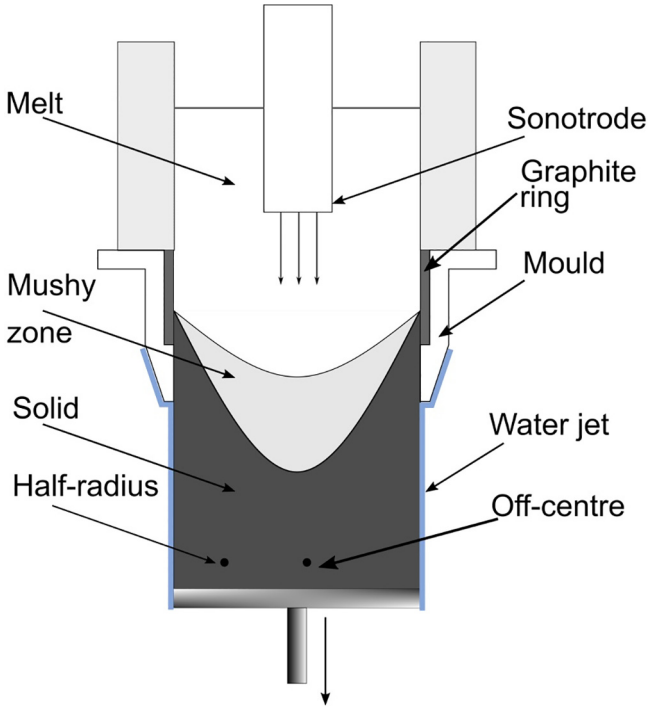

Fig. 1. Schematic diagram of ultrasonic treatment of the direct-chill casting process. A sonotrode is inserted in the hop-top of a conventional DC casting setup. The two dots roughly denote the half-radius and off-centre position (15 mm from axis) of the billet. In the validation experiment, the samples are observed from a section near the middle of the cast length.

model of grain growth consisting of the solid, inter-dendritic liquid, and extra-dendritic liquid to model macrosegregation and the effect of grain refiners in DC casting. While their model provides a better understanding of coupling of microstructure and macrosegregation at the process scale, more work is required to adequately explain the macrosegregation mechanism. Tveito et al. [9] developed a simplified three-phase model that is applicable to equiaxed solidification and established that grain morphology must be correctly described to obtain accurate macrosegregation predictions. These models are not currently considered in this work but will be implemented at a later stage to quantify the effect of ultrasound on macrosegregation.

While DC casting modelling has been successful in the literature, acoustic streaming modelling is more difficult, and even more so in the presence of acoustic cavitation and turbulence. Acoustic cavitation models are based upon the set of equations derived by van Wijngaarden [10] which developed a set of non-linear equations to model flow in bubbly liquids in the presence of moderate pressure oscillations. While van Wijngaarden developed these equations through physical reasoning, Caflisch et al. [11] mathematically re-derived these equations based on Foldy's approximation [12]. This model is valid at slow flow fields because it neglects convection and assume that the bubbles are disperse, i.e. is valid far from the sonotrode. Lebon et al. [13] used such a model to compute the acoustic pressures in water and aluminium and obtained a good agreement with measured values. However, this set of non-linear equations is computationally expensive to solve and require the solution of ordinary differential equations that describe bubble dynamics in each computational cell. This requirement makes the Caflisch model inadequate for optimization studies with the current computational power available.

Recent advances to model the non-linear effect of bubbles on sound propagation has led to computationally tractable formulations. The starting point of these types of model is from the linear model of Commander and Prosperetti [14]. Their linearized model incorporated the mixture effect through a complex wave number in a Helmholtz equation. However, this model is applicable at low pressures where the bubbles oscillate linearly. Non-linear effects due to acoustic cavitation were considered by Louisnard [15] who used the Rayleigh-Plesset equation to derive the attenuation term in the complex wave. This term depends on pressure making the pressure propagation equation non-linear. This method was extended by Jamshidi and Brenner who used the Keller-Miksis equation instead to consider compressibility in the bubble dynamics: this effect cannot be neglected because energy dissipation due to acoustic radiation is of the same order of magnitude as thermal dissipation [16]. The non-linear and linear models were compared by Dogan and Popov [17] who established that the non-linear models more adequately represent the effect of attenuation in bubbly liquids. While Louisnard [15] assumed that the real part of the wave number was given by the linear approximation, Trujillo [18] rigorously re-derived a non-linear model and validated his formulation at low pressure amplitudes. His derivation revealed that the real part of the wave number is related to the average acoustic energy while the imaginary part is related to average energy dissipation.

These recent development in non-linear pressure propagation theory has enabled the emergence of an acoustic streaming model that properly accounts for the effect of cavitation bubbles. Louisnard [19] coupled his non-linear model to the Reynolds-Averaged Navier Stokes equations and modelled turbulent flow in the presence of cavitation and obtained good agreement with a Particle Image Velocimetry (PIV) experiment in water. In this paper, we apply Louisnard's acoustic streaming model [19] coupled with Trujillo's non-linear Helmholtz equation [18] to the ultrasonic treatment in DC casting (USDC) of an AA6XXX series aluminium alloy to predict the acoustic streaming pattern in the sump. This model extends our previously validated model of acoustic streaming in water [20] by including the heat transfer and species conservation equations and considering the effect of acoustic radiation in non-linear pressure propagation. Results are presented for two configurations: with the sonotrode either submerged to the level of the graphite ring or positioned 100 mm above the graphite ring level, for which experimental measurements of grain size and dendrite arm spacing are available [21]. Both configurations result in larger temperature gradients across the reduced width of the transition region and larger cooling rates near the centre of the billet. Results show that the flow effect is weaker for the higher position, resulting in less melt penetration into the slurry.

2. Theory

2.1. Acoustic streaming model

Denoting the harmonic part of acoustic pressure p as $\Re(Pe^{i\omega t})$, the complex amplitude P is approximately described by the nonlinear Helmholtz equation [19]

$$\nabla^2 P + K^2 P = 0, \tag{1}$$

where the real and imaginary parts of K^2 are given by

$$\Re(K^2) = \frac{\omega^2}{c^2} - \frac{\mathscr{A}}{|P|}, \tag{2}$$

$$\Im(K^2) = -\frac{\mathscr{B}}{|P|}, \tag{3}$$

where ω is the angular frequency, c is the speed of sound in the pure liquid, and the terms $\mathscr{A}$ and $\mathscr{B}$ derived by Trujillo as [18] as either

$$\mathscr{A} = -\frac{\rho\omega^2}{\pi}\int_0^{2\pi} \frac{\partial^2\beta}{\partial\tau^2}\cos\left(\tau + \frac{\pi}{2}\right)d\tau, \tag{4}$$

$$\mathscr{B} = \frac{\rho\omega^2}{\pi}\int_0^{2\pi} \frac{\partial^2\beta}{\partial\tau^2}\sin\left(\tau + \frac{\pi}{2}\right)d\tau, \tag{5}$$

or

$$\mathscr{A} = -\frac{\rho\omega}{\pi}\int_0^{2\pi}\frac{\partial\beta}{\partial\tau}\sin\left(\tau+\frac{\pi}{2}\right)d\tau, \tag{6}$$

$$\mathscr{B} = -\frac{\rho\omega}{\pi}\int_0^{2\pi}\frac{\partial\beta}{\partial\tau}\cos\left(\tau+\frac{\pi}{2}\right)d\tau. \tag{7}$$

ρ is the pure liquid density. τ denotes time within one period between [0, 2π]. The bubble volume fraction β is given by

$$\beta = \frac{4}{3}\pi R^3 N = VN, \tag{8}$$

where R is the bubble radius and $V = \frac{4}{3}\pi R^3$ is the bubble volume. The bubble density N is assumed to follow the step function

$$N = \begin{cases} N_0 & \text{if } |P| > P_B \\ 0 & \text{if } |P| \le P_B \end{cases}, \tag{9}$$

where the Blake threshold $P_B = p_0\left[1+\sqrt{\frac{4}{27}\frac{S^3}{1+S}}\right]$, where $S = \frac{2\sigma}{p_0 R_0}$, R_0 being the bubble equilibrium radius.

The terms $\mathscr{A}$ and $\mathscr{B}$ are estimated from the solution of a bubble dynamics equation. This work follows the approach of Trujillo [18] by adopting the Keller-Miksis equation to account for dissipation due to acoustic radiation: this effect is considered to yield a periodic solution to the evolution of bubble dynamics:

$$\rho\left[\left(1-\frac{\dot R}{c}\right)R\ddot R + \frac{3}{2}\left(1-\frac{\dot R}{3c}\right)\dot R^2\right] = \left(1+\frac{\dot R}{c}+\frac{R}{c}\frac{d}{dt}\right)\left[p_g + p_v - \frac{2\sigma}{R} - \frac{4\mu\dot R}{R} - p_0\{1 - A\sin(\omega t)\}\right], \tag{10}$$

σ is the surface tension between the liquid and gas phases, μ is the dynamic viscosity of the liquid, p_0 is the pressure at infinity (set to atmospheric pressure), A is the pressure amplitude (normalized by p_0) of the excitation source of angular frequency ω, and p_v is the vapour pressure.

The gas pressure p_g is evaluated by solving the differential equation

$$\frac{dp_g}{dt} = \frac{3}{\mathrm{R}}\left[(\gamma-1)\left(k\frac{dT}{dr}\bigg|_{r=R}\right) - \gamma p_g\dot R\right], \tag{11}$$

which takes into account the effect of heat transfer during bubble pulsation [16,22]. k is the heat conductivity of the hydrogen gas. The gas pressure at the equilibrium radius R_0, denoted by $p_{g,0}$, is used as the initial value for Eq. (11). Assuming adiabatic pulsation, the polytropic exponent is $\gamma = 1.4$, the ratio of specific heats.

Since the vapour pressure of aluminium at its melting point is 0.000012 Pa [23], aluminium vapour bubble formation is highly unlikely and the vapour pressure for modelling purposes can be approximated as zero. Therefore, no vapour transfer equation is coupled with the Keller-Miksis equation. Also, rectified diffusion of hydrogen bubbles is a slow process [1] as evidenced by empirical observation of stably cavitating bubbles by X-ray radiography [24]. Therefore, the transfer of hydrogen into cavitating bubbles is also neglected.

Employing the method of Toegel et al. [25], the temperature gradient at the bubble surface, required in the evaluation of Eq. (11), is approximated linearly as

$$\frac{dT}{dr}\bigg|_{r=R} = \frac{T-T_\infty}{\sqrt{(RD)/\{3(\gamma-1)\dot R\}}}, \tag{12}$$

where D is the diffusivity of the gas [16]. The temperature of the liquid bulk T_∞ is approximated as the inlet temperature. The temperature of the gas inside the bubble, T, is evaluated using the first law of thermodynamics

$$C_v\dot T = 4\pi R^2 k\frac{T_\infty - T}{l_{th}} - p_g\dot V, \tag{13}$$

where $l_{th} = \min\left(\frac{R}{\pi}, \sqrt{\frac{RD}{\dot R}}\right)$ is the thermal diffusion length and C_v is the specific heat capacity of the gas.

2.2. DC casting model

A continuum formulation is used to present the DC casting problem. The mass conservation equation is

$$\frac{\partial\rho}{\partial t} + \nabla\cdot(\rho\boldsymbol{u}) = 0, \tag{14}$$

where $\boldsymbol{u}$ is the velocity of the liquid phase.

The energy balance equation is

$$\frac{\partial(\rho h)}{\partial t} + \nabla\cdot(\rho\boldsymbol{u}h) = \nabla\cdot(\kappa\nabla T) - L_f\left[\frac{\partial(\rho f_l)}{\partial t} + \nabla\cdot(\rho\boldsymbol{u}f_l)\right], \tag{15}$$

where $h = C_pT$ is the enthalpy, κ is thermal conductivity, T is temperature, C_p is specific heat capacity, L_f is latent heat of fusion, and f_l is the volume fraction of liquid. The source term in Eq. (15) is due to phase change [26].

The species conservation equation is given by

$$\frac{\partial(\rho C^s)}{\partial t} + \nabla\cdot(\rho\boldsymbol{u}C^s) = \nabla\cdot(\rho f_l D_l^s\nabla C^s) + \nabla\cdot\{\rho f_l D_l^s\nabla(C_l^s - C^s)\} - \nabla\cdot\{\rho(\boldsymbol{u}-\boldsymbol{u}_s)(C_l^s - C^s)\}, \tag{16}$$

where $\boldsymbol{u}_s$ is the velocity of the solid shell which is set as the casting speed, C^s is the concentration of species s, and D_l^s is the diffusivity of species s in the liquid. The liquid concentration is calculated using the lever rule

$$C_l^s = \frac{C^s}{\{(1-f_l)k_p + f_l\}}, \tag{17}$$

where k_p is a binary partition coefficient.

It is conventional to divide the transition region (between liquidus and solidus) into a slurry (above the coherency isotherm) and a mush (below the coherency isotherm) [5]. The momentum conservation equation in the liquid and slurry region ($g_c \le f_l \le 1$) is given by

$$\frac{\partial(\rho\boldsymbol{u})}{\partial t} + \nabla\cdot(\rho\boldsymbol{u}\boldsymbol{u}) = \nabla\cdot(\mu\nabla\boldsymbol{u}) - \nabla p + \rho_b\boldsymbol{g} + \boldsymbol{f}, \tag{18}$$

where $\mu = \mu_t + \mu_{l,m}$ is the effective viscosity, p is pressure, and $\boldsymbol{g}$ is the acceleration due to gravity. $\boldsymbol{f}$ represents the force driving acoustic streaming, and g_c is the liquid fraction reflecting the coherency,

$$\boldsymbol{f} = -\nabla(\rho_l\boldsymbol{v}\otimes\boldsymbol{v}), \tag{19}$$

where $\boldsymbol{v} = \frac{\nabla\mathrm{P}}{\rho\omega}$ is the acoustic velocity that is estimated by solving the equation for sound propagation only [27]. Once this acoustic velocity is estimated, the flow velocity $\boldsymbol{u}$ can be calculated by solving Eq. (18). The overbar indicates that the values are obtained from averaging over a period of the acoustic bubble.

The buoyancy term is evaluated in assuming the Boussinesq approximation, i.e.

$$\rho_b\boldsymbol{g} = \rho_{ref}\boldsymbol{g}\left[\beta_T(T-T_{ref}) + \sum_s\beta_s(C_l^s - C_0^s)\right], \tag{20}$$

where β_T is the thermal expansion coefficient and β_s is the solution expansion coefficient for species s.

In the slurry region, the viscosity is modified to simulate flow with resistance due to the presence of the grains

$$\mu_{l,m} = \mu_l/\left\{1 - F_\mu\frac{(1-f_l)}{A_c}\right\}^2, \tag{21}$$

where F_μ is a switching function and A_c is a crystal constant [28].

In the mushy zone and solid regions ($0 \le f_l \le g_c$), the momentum conservation equation is given by

$$\frac{\partial(\rho \boldsymbol{u})}{\partial t} + \nabla\cdot(\rho \boldsymbol{u}\boldsymbol{u}) = \nabla\cdot(\mu\nabla \boldsymbol{u}) - \nabla p + \rho_b \boldsymbol{g} - (\boldsymbol{u} - \boldsymbol{u}_s)\frac{(1-f_l^2)}{f_l^3}K, \tag{22}$$

where K is the permeability coefficient. The last term of Eq. (22) is a Carman-Kozeny source term that accounts for the resistance to flow in the mushy/solid region.

The $k-\omega$ shear stress transport (SST) model is used for closure:

$$\frac{\partial(\rho k)}{\partial t} + \nabla\cdot(\rho \boldsymbol{u} k) = \nabla\cdot(\rho D_k \nabla k) + \rho G - \frac{2}{3}\rho k(\nabla\cdot \boldsymbol{u}) - \rho\beta^*\omega k, \tag{23}$$

$$\frac{\partial(\rho\omega_t)}{\partial t} + \nabla\cdot(\rho \boldsymbol{u}\omega_t) = \nabla\cdot(\rho D_\omega \nabla\omega_t) + \frac{\gamma\rho G}{\nu} - \frac{2}{3}\gamma\rho\omega_t(\nabla\cdot \boldsymbol{u}) - \rho\beta_\omega\omega_t^2 - \rho(F_1 - 1)CD_{k\omega}. \tag{24}$$

The turbulent viscosity is given by

$$\mu_t = a_1\frac{\rho k}{\max(a_1\omega_t,\, b_1 F_{23}\boldsymbol{S})}. \tag{25}$$

k is the kinetic energy of turbulence. ω_t is the dissipation rate. The turbulent model coefficients are identical to those in the original reference [29].

3. Setup

3.1. Geometry of ultrasonic melt treatment in DC model

Fig. 1 illustrates the ultrasonic treatment process. A 24 mm Ø sonotrode is inserted along the axis of a 155 mm Ø DC casting mould and introduces power ultrasound in the sump. The inlet is set to 50 mm above the sonotrode tip: Reese [30] established that the temperature is stratified in the sump, and as such the inlet temperature can be fixed to the liquidus temperature of the melt and the feeding does not have to be explicitly modelled. The graphite ring depth is 40 mm, followed by a 17 mm deep water cooled aluminium mould. The water jet flow rate is 60 L/min with an average temperature of 20 °C. The sonotrode is connected to a magnetostrictive transducer supplying 2.0 kW of power at $f = 17.3$ kHz: this corresponds to an estimated amplitude of $y = 20$ µm peak-to-peak. The sonotrode is located at two positions in the sump: (i) submerged to the level of the graphite ring and (ii) at 100 mm above the graphite ring level. This setup corresponds to the experiment described in [21].

3.2. Material properties and model parameters

The material properties for an A6060 alloy (composition in Table 1 and solutal properties in Table 2) were calculated using the National Physical Laboratory's (NPL) Virtual Measurement System (VMS) [31] and the Pro-CAST material property calculator [32]. For the specific heat capacity, the values in the transition region were calculated using the method of mixtures. Other parameters are listed in Table 3.

3.3. Numerical implementation

The finite volume solver *buoyantPimpleFoam* from the open source package OpenFOAM 5.x [33] was modified as described in this section. The discretization schemes and solver control parameters are listed in Table 4. The boundary conditions for the model are presented in Fig. 2 and Table 5. The sonotrode is sufficiently far from the solidification front so that the expected intensive cavitation zone does not interact with growing dendrites.

Table 1
Composition of an A6060 alloy for material properties calculation in VMS.

Element	Al	Si	Mg	Fe	Mn	Cu	Zn	Ti
Composition (mass %)	98.65	0.45	0.475	0.2	0.05	0.05	0.075	0.05

3.4. Secondary cooling heat transfer boundary condition

The heat transfer coefficient at the mould and water-cooled mould is estimated from Rohsenow's formula [34] and entered as a table at the wall. The tabular boundary condition is implemented by modifying the *compressible: externalWallHeatFluxTemperatureFvPatchScalarField* class to read an interpolation table. Material properties for water are given in Table 6.

The heat transfer coefficient is evaluated as

$$h = \begin{cases} h_{conv} & \text{if } q''_{incp} \leqslant q''_{conv} \\ h_{conv} + h_{boil} & \text{if } q''_{incp} > q''_{conv} \end{cases} \tag{26}$$

where the heat transfer at incipient boiling is given by

$$q''_{incp} = 3910\ \Delta T^{2.16} \tag{27}$$

The forced-convection heat transfer coefficient is evaluated as [36]

$$h_{conv} = 0.01\mathrm{Pr}^{\frac{1}{3}}\left(\frac{4\Gamma}{\mu}\right)^{\frac{1}{3}}\left(\frac{\mu^2}{k^3{\rho_l}^2 g}\right)^{\frac{1}{3}}, \tag{28}$$

where $Pr = \frac{C_p\mu}{k}$ is the Prandtl number.

The effect of nucleate boiling is accounted for by

$$q''_{boil} = h_{boil}(T - T_{water}) = \mu L_v\sqrt{\frac{g(\rho_l - \rho_v)}{\sigma}}\left(\frac{C_p\Delta T}{L_v\overset{n}{\mathrm{Pr}}\ C_{sf}}\right) \tag{29}$$

3.5. Solution of the nonlinear Helmholtz equation

Special consideration is given to the implementation of the solution of the Helmholtz Eq. (1), which is not straight-forward:

1. The Keller-Miksis equation (10), gas pressure equation (11), and first law of thermodynamics equation (13) are solved for a cavitating hydrogen bubble with equilibrium radius $R_0 = 5$ µm for a range of pressures including the pressure below the sonotrode at the operating power. The material properties for the hydrogen gas are given in Table 7. This pressure is estimated from measurements in experiments featuring a similar transducer using a calibrated high-temperature cavitometer [37].
2. The values of $\mathscr{A}$ and $\mathscr{B}$ at the operating pressure are obtained over a period of oscillation using the formulae derived in [18] after a periodic equation is obtained. Periodicity is established when the Eqs. (4)–(7) yield identical values for both $\mathscr{A}$ and $\mathscr{B}$. These values are entered as transport properties of the Helmholtz equation solver. The following steps are looped over the run time. Even if a final steady state regime is expected, solving transient equations results in greater numerical stability due to the transient term acting like an inertial relaxation term in the flow equations. For each time step:
   a. Eq. (1) is split into two equations for the real and imaginary parts of P.

$$\nabla^2\Re(P) + \frac{\omega^2}{c^2}\Re(P) = \mathscr{A} \tag{30}$$

$$\nabla^2\Im(P) + \frac{\omega^2}{c^2}\Im(P) = \mathscr{B} \tag{31}$$

   b. Eqs. (30) and (31) are solved sequentially using the finite volume method. Convergence is achieved only with a suitable use of preconditioners for both equations, i.e. Simplified Diagonal-based Incomplete Cholesky preconditioner (DIC) with DIC smoothing followed by Gauss-Seidel (DICGaussSeidel).
   c. The computed values of acoustic pressure are used in the acoustic

Table 2
Solutal properties for an A6060 alloy.

Solute	Si	Mg	Fe	Mn	Cu	Zn	Ti
Partition coefficient k_p	0.10	0.32	0.02	0.63	0.13	0.32	0.12
Liquid diffusivity D_l ($m^2 s^{-1}$)	3×10^{-9}	3×10^{-9}	3×10^{-9}	3×10^{-9}	3×10^{-9}	3×10^{-9}	3×10^{-9}
Solution expansion coefficient β	-3.7×10^{-4}	1.3×10^{-4}	-4.6×10^{-3}	-1.0×10^{-3}	-1.2×10^{-3}	-1.3×10^{-3}	-4.5×10^{-4}

Table 3
Model parameters for the DC casting simulation of an A6060 alloy.

Parameter	Quantity
Casting velocity $\boldsymbol{u}_s$ (m s^{-1})	(0, 0, −0.002917)
Inlet temperature (K)	933
Liquidus temperature T_l (K)	929.250
Solidus temperature T_s (K)	757.375
Latent heat L_f (J kg^{-1})	375696.0
Thermal expansion coefficient β (K^{-1})	23×10^{-6}
Mushy region momentum sink coefficient K (s^{-1})	1.522×10^{7}
Density ρ (kg m^{-3})	2375
Speed of sound c (m s^{-1})	4600
Kinematic viscosity ν ($m^2 s^{-1}$)	5.5×10^{-7}
Maximum Courant number	0.5

Table 4
OpenFOAM discretization schemes and solver control parameters.

Discretization schemes	
ddtSchemes	Euler
gradSchemes	
default	cellLimited Gauss linear 1
grad($\Im(P)$), grad($\Re(P)$)	Gauss linear
grad(ρ)	cellLimited leastSquares 1
divSchemes	
default	bounded Gauss linear
div(u), div(h), div(f_l)	bounded Gauss limitedLinear 1
div(C^S)	bounded Gauss upwind
laplacianSchemes	
default	Gauss linear corrected
interpolationSchemes	
default	linear
snGradSchemes	
default	corrected
Solver control parameters	
$\Im(P)$, $\Re(P)$	PCG, DILU Preconditioner DIC, DICGaussSeidel with cacheAgglomeration
All other variables	PBiCGStab, DIC/DILU
momentumPredictor	No
nOuterCorrectors	7
nCorrectors	1
nEnergyCcorrectors	7
nNonOrthogonalCorrectors	0

source term (19) of the momentum equation.

4. Results and discussion

An axisymmetric model of the USDC setup described in Fig. 1 is run in the custom OpenFOAM solver whose implementation was described in the previous section. This model has been implemented in version 5.x. The model is first run without the sonotrode, but with the same operating conditions, to obtain the initial conditions for the USDC simulations. The results from this conventional DC casting simulation are also compared with the USDC results.

The period-averaging assumption to calculate $\mathscr{A}$ and $\mathscr{B}$ makes the proposed model computationally cheap, since this stage negates the prohibitive use of very fine time steps that are required in van Wijngaarden-type models. The current results have been run with time steps of the order of 0.01 s, resulting in run times of around 9 h until convergence on a 16 core (3.0 GHz) CPU. These run times make this model attractive for optimization and uncertainty quantification studies.

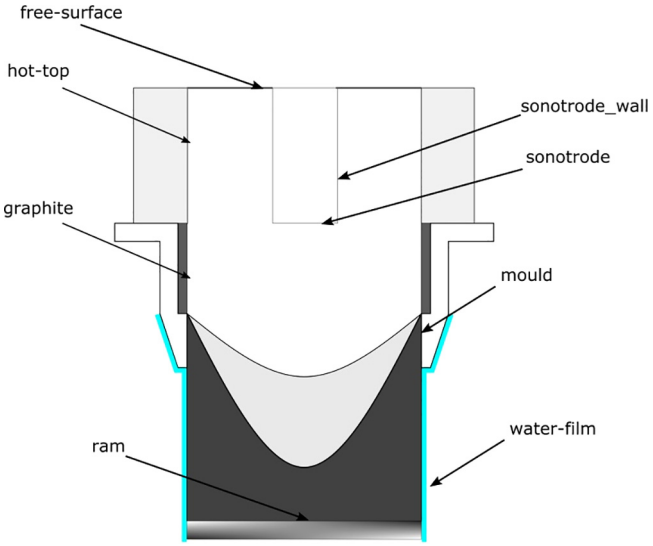

Fig. 2. Boundary conditions for ultrasonic melt treatment DC casting simulations.

4.1. Evaluation of attenuation terms

The coupled Eqs. (10), (11), and (13) are solved for hydrogen bubbles of equilibrium radius 5 μm cavitating due to sinusoidal forcing signals of frequency 17.3 kHz and amplitudes in the range $0.3 \leq A \leq 10$. A bubble density of $N_0 = 1.9 \times 10^9$ is assumed, corresponding to the range of bubble fraction β for which the numerical model is stable [20]. This system of non-linear equations is solved using the ODE solver supplied by the SciPy Python library [38]. Because of the stiffness of the problem, the Adams/BDF method with automatic stiffness detection and switching [39] is used.

$\mathscr{A}$ and $\mathscr{B}$ are evaluated using Eqs. (4)–(7). The integrals are evaluated in the last cycle: to ensure that the evaluation is precisely performed in the last cycle, the ODE solution is output at 400 regularly spaced intervals per cycle and only the solution in the last cycle comprising the 400 last values of R and $\dot{R}$ is used. The variation of the attenuation terms, normalized by bubble volume fraction, with forcing amplitude A is given in Fig. 3. The required values of $\mathscr{A}$ and $\mathscr{B}$ for the ultrasonic processing simulation are interpolated using splines of order 3 assuming $A = 2.4$, the expected average pressure under the horn based on previous measurements in aluminium processing [13].

4.2. Mesh convergence analysis

The converged mesh density for the numerical simulations is determined by running the DC casting model for three different mesh densities and evaluating an estimate of the continuum solution of the

Table 5
Boundary conditions.

u	
Ram	Fixed value (0, 0, −0.002917) m s^{-1}
water-film|mould|graphite|ceramic|hot-top|sonotrode|sonotrode_wall	No slip
free-surface	Normal gradient = 0
p	
Ram	Fixed flux pressure, value = 101325.0 Pa
free-surface	Fixed value 101325.0 Pa
water-film|mould|graphite|ceramic|hot-top| sonotrode|sonotrode_wall	Fixed flux pressure, value = 101325.0 Pa
T	
Ram	Inlet-Outlet, internal value when inflow, normal gradient = 0 when outflow
free-surface	Fixed value, 933 K
hot-top| sonotrode|sonotrode_wall	Normal gradient = 0 (adiabatic)
water-film|mould|graphite|ceramic	Heat transfer coefficient prescribed from a lookup table, values calculated from [34] External temperature = 293.0 K
k	
ram	Normal gradient = 0
free-surface	Fixed value 5.58 × 10^{-8} m^2s^{-2}
water-film|mould|graphite|ceramic|hot-top| sonotrode|sonotrode_wall	class *kqRWallFunction*, Normal gradient = 0
ω_t	
ram	Normal gradient = 0
free-surface	Fixed value 0.001 s^{-1}
water-film|mould|graphite|ceramic|hot-top| sonotrode|sonotrode_wall	class *omegaWallFunction*, computed as sqrt(ω_visˆ2 + ω_logˆ2) [35]
$\Re(P)\|\Im(P)$	
water-film|mould|graphite|ceramic|hot-top| sonotrode_wall	Normal gradient = 0 Pa m^{-1}
free-surface	Fixed value = 0 Pa
sonotrode	Fixed gradient = $\omega\rho v_n/\sqrt{2} = \omega^2\rho y/\sqrt{2}$ with amplitude y assumed to be 10 μm.

Table 6
Water properties at saturation temperature [36].

Property	Quantity
Saturation temperature (K)	372.8
Liquid density ρ_l (kg m^{-3})	958.6
Vapour density ρ_v (kg m^{-3})	0.5903
Latent heat of vaporization L_v (J kg^{-1})	2257000.0
Thermal conductivity k (W m^{-1} K^{-1})	0.6790
Specific heat capacity C_p (J kg^{-1} K^{-1})	4215
Surface tension σ (N m^{-1})	0.059
Flow rate per unit circumference Γ (m^2 s^{-1})	0.00308
Nucleate boiling constant C_{sf}	0.011

Table 7
Hydrogen gas bubble properties [1]. Unavailable properties were approximated by those of air.

Property	Quantity
Initial bubble radius R_0 (μm)	5
Bubble density N_0 (m^{-3})	1.9 × 10^9
Equilibrium pressure p_0 (Pa)	101325.0
Gas diffusivity D (m^2 s^{-1})	1.7 × 10^{-4}
Polytropic coefficient$\varkappa$	1.4
Thermal conductivity k (mW m^{-1} K^{-1})	24.35
Specific heat capacity C_v (J kg^{-1} K^{-1})	717
Surface tension σ with aluminium melt (N m^{-1})	0.86
Vapour pressure p_v (MPa)	0.0

temperature field using the Richardson Extrapolation method. Fig. 4 shows the grid refinement analysis for the case using the predicted centre line temperature: the solution evaluation on a mesh of 20,736 cells, corresponding to an average cell length of 1 mm, is grid independent. This mesh density is used for all the results presented in this work.

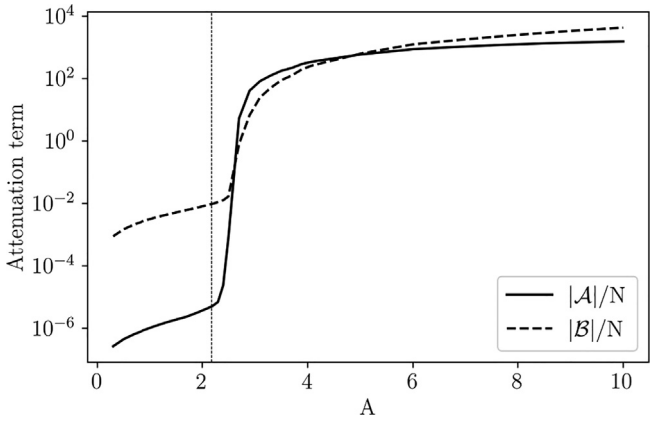

Fig. 3. Estimated attenuation terms divided by bubble density. The vertical dash-dotted line represents the Blake pressure.

4.3. Treatment with the sonotrode aligned with the graphite ring

Fig. 5 shows the effect of ultrasonic treatment on the sump when the sonotrode is submerged down to the level of the graphite ring (as in Fig. 2) by comparing the sump profile in conventional DC casting (left) with the modified profile with acoustic streaming (right). A strong central acoustic streaming jet (see Fig. 6 left) depresses the liquidus and shortens the transition zone in the centre of the billets, thereby drastically increasing the temperature gradient in the transition region. The flow is opposite to the natural convection direction and the melt flows upwards, parallel to the solidification front towards the mould. The transition zone is also depressed at the sides, leaving a larger

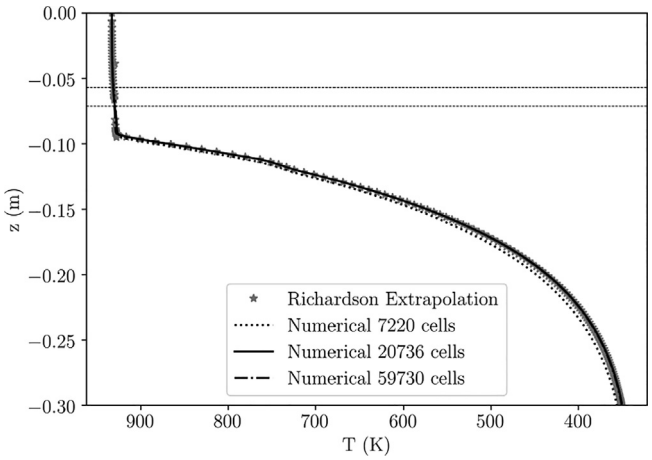

Fig. 4. Mesh independence analysis of DC casting simulation using the centre line temperature. The case with 20,736 cells is grid independent.

temperature gradient compared with conventional DC casting (Fig. 8).

The acoustic pressure decays exponentially below the sonotrode, as shown in Fig. 6 (right) and Fig. 7. This prediction is consistent with pressure measurements in a crucible [40]. Due to acoustic shielding and energy dissipation of the acoustic wave, most of the ultrasound energy is consumed inside the cavitation zone [41]. With the cavitation zone being active only below the sonotrode, this implies that the acoustic streaming pattern could be the main mechanism behind the grain morphology modification in the sump.

In Fig. 9, the cooling rate $\dot{T}$, defined here as $\nabla T \cdot (\boldsymbol{u} - \boldsymbol{u}_s)$, inside the slightly elevated sump is larger in the centre of the billet due to the large speed jet impinging directly from under the sonotrode and the larger temperature gradient in the shortened transition zone. This increase implies an increase in the solidification velocity. These large cooling rates result in smaller dendrite arm spacing λ [28] compared with the DC casting case without ultrasound.

4.4. Treatment with the sonotrode positioned 100 mm above the graphite ring

With the sonotrode elevated 100 mm above the graphite ring level, the flow pattern is similarly reversed at the centre, as shown in Fig. 10. However, the sump becomes somewhat shallower as compared with the sonotrode at the graphite ring level (Fig. 11). Therefore, with a weaker penetration jet, solidification occurs faster than with the sonotrode at the lower position. The temperature gradients are of the same order of magnitude (Fig. 12).

When the sonotrode is located 100 mm above the graphite ring level, the predicted cooling rates are lower than those obtained when the sonotrode is aligned with the graphite ring level, as shown in Fig. 13. This implies that the dendrite arm spacing at the centre of the billet will be larger when the horn in the elevated position, but still smaller than in the reference case.

4.5. Verification of simulation results with the microstructure observations

A cast billet of an AA6XXX-series alloy was cut in the horizontal direction in the middle of the cast length. The observed samples are taken from the off-centre and half-radius locations (schematically illustrated in Fig. 1). Details of the experiment can be found elsewhere [21].

Left parts of Figs. 15 and 16 show the grain morphology at half radius of the billet when the ultrasonic sonotrode is located at the graphite ring level (Fig. 15) and 100 mm above the graphite ring level, respectively (Fig. 16). When the sonotrode is located at the lowest position in the hot top, closer from the solidification front, a non-dendritic, very fine grain structure is obtained at half radius. The strong liquid flow penetrating into the semi-solid region predicted by our simulations in Fig. 5 could explain that dendrite fragments and free grains can be transported from the centre of the sump toward the half radius of the billet resulting in the small grain size. Both cases show a clear grain refinement compared with the reference cast without ultrasound (Fig. 14). Grain refinement is more pronounced in Fig. 15, consistent with the stronger velocities, deeper penetration into the slurry region (which facilitates fragmentation and transport of fragments) and higher cooling rates (that facilitate structure refinement) demonstrated in the numerical model for the lower position of the sonotrode (Fig. 9).

Note the interesting dendritic growth towards the sonotrode position in Fig. 15 (right). The numerical simulations predicted the acoustic streaming pattern as shown in Fig. 5. When the strong jet penetrates the transition zone, hot melt is brought into the solidification front from the sonotrode, lowering the liquidus position in the sump and dramatically increasing the temperature gradient at the solidification front.

Studies of dendritic grains growing under the conditions of forced flow has been explored experimentally, as well as numerically by phase field simulations [42]. They conclude that dendrites will grow upstream towards the fluid flow, developing elongated dendritic grains. There is a clear shift from unconstrained to constrained growth [43], leading to more elongated grains, when the sonotrode is at its lowest position thus increasing the temperature gradient at the solid–liquid interface. In situ X-ray investigation of aluminium alloy solidification showed that when the cooling rate is not high enough, grains tend to elongate in the direction of the temperature gradient [44].

The dendrites shown in Fig. 15 grew preferentially towards the incoming melt flow created by the acoustic streaming. However, this was

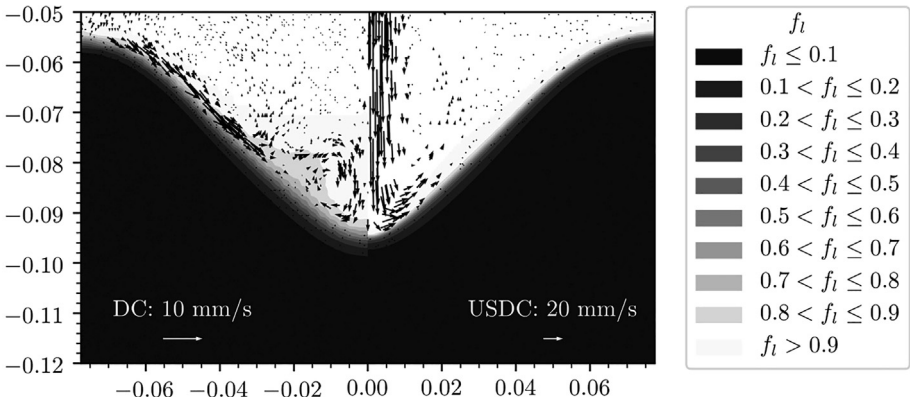

Fig. 5. Comparison of the sump profiles between conventional DC casting (left) and USDC (right) with the sonotrode submerged to the level of the graphite ring. f_l is the liquid fraction. Arrows are shown for the scale of velocity.

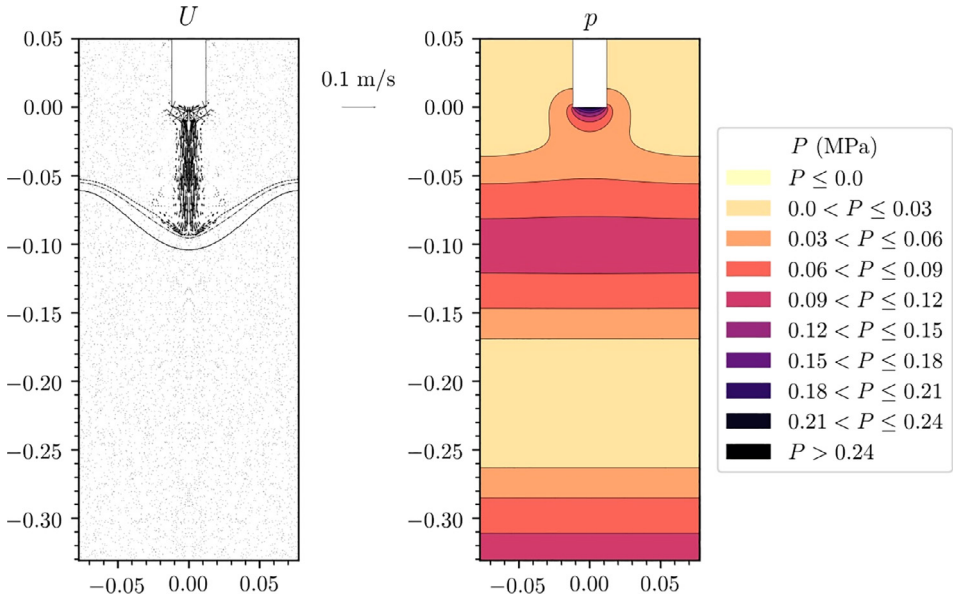

Fig. 6. Velocity (left) and acoustic pressure (right) fields in USDC casting billet with the sonotrode submerged to the level of the graphite ring.

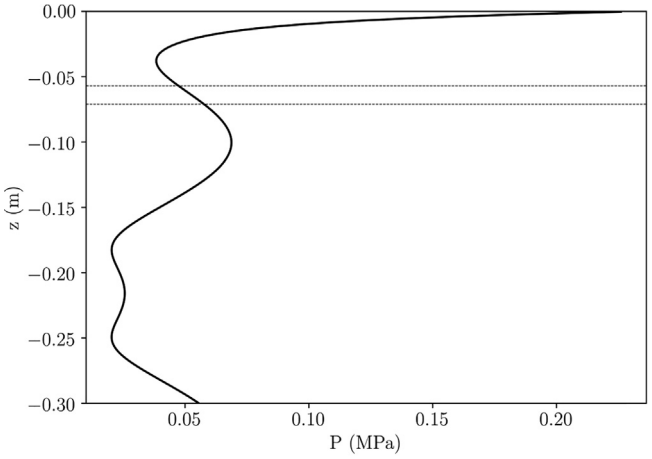

Fig. 7. Acoustic pressure along the centre line of the billet. The acoustic pressure decays exponentially under the sonotrode.

not pronounced when the sonotrode was located 100 mm higher, with the incoming jet and the flow parallel to the solidification front being considerably weaker than when the sonotrode was placed at the graphite ring level (Fig. 11). The higher temperature gradient in the centre of the billet would also reduce the solidification time at this location in the billet, generating significantly smaller secondary dendrite arm spacing λ_2 than the reference cast as shown in Fig. 17 (measurements from the centre of the billet) and elsewhere [21]. These dendrite arm spacing measurements are in agreement with the prediction of larger cooling rates in the sump in Figs. 9 and 13.

5. Conclusions

A novel acoustic streaming model applicable to the ultrasonic melt processing integrated in the direct-chill casting process has been presented for the first time. The model is numerically stable, representative of the physics of acoustic cavitation in the melt, and is in qualitative agreement with the grain morphology modification of ultrasonic treatment of billets:

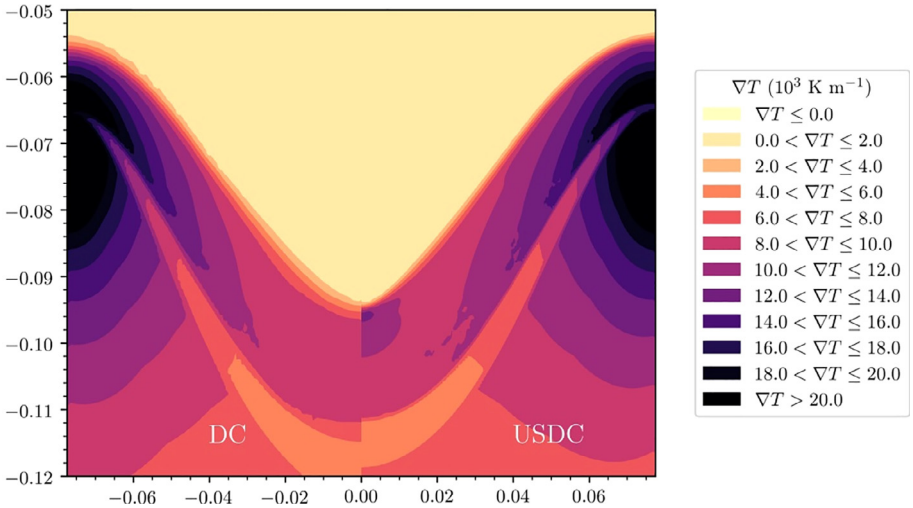

Fig. 8. Comparison of the temperature gradients between conventional DC casting (left) and USDC (right) with the sonotrode submerged to the level of the graphite ring.

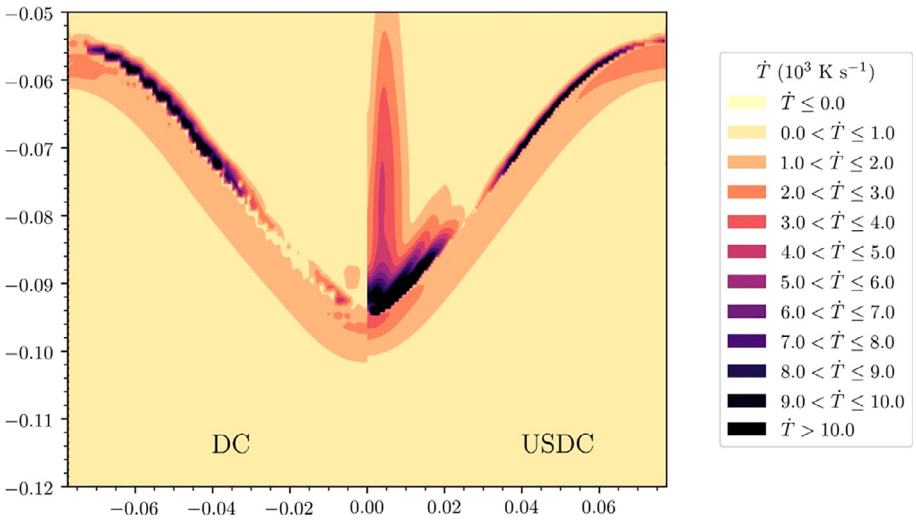

Fig. 9. Comparison of the cooling rates between conventional DC casting (left) and USDC (right) with the sonotrode submerged to the level of the graphite ring.

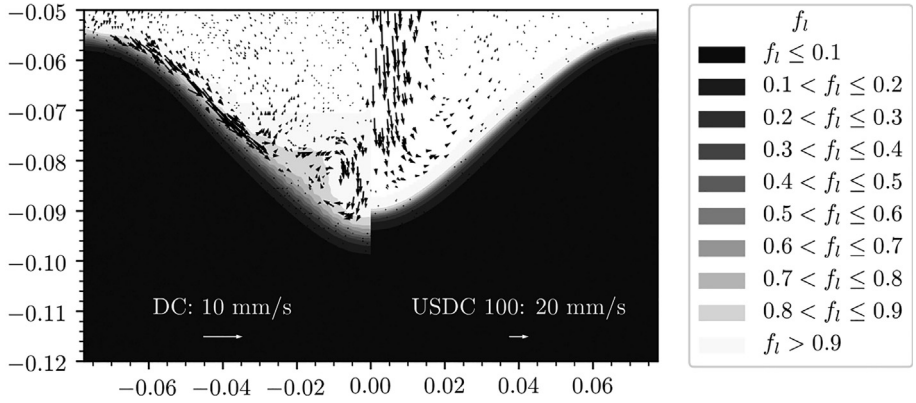

Fig. 10. Comparison of the predicted liquid fractions and sump profiles between conventional DC casting (left) and USDC (right) with the sonotrode positioned 100 mm above the graphite ring. Arrows are shown for the scale of velocity.

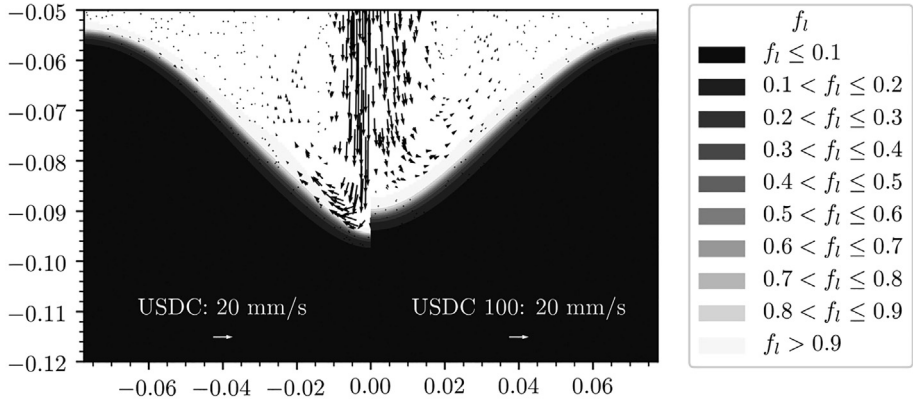

Fig. 11. Comparison between sump profiles in USDC casting with the sonotrode (left) submerged to the level of the graphite ring and (right) positioned 100 mm above the graphite ring.

1. The model is computationally attractive: the period averaging assumption negates the use of fine time steps as is required in van Wijngaarden type models. This makes the proposed model suitable for optimization studies.
2. Ultrasound modifies the sump profile by depressing the slurry region along the axis of the billet and pushing the slurry sideways along the solidification front. This contributes to the transport of floating grains towards the melt and increases the temperature gradient in the phase transition region.
3. The sonotrode position affects the acoustic streaming pattern and grain morphology accordingly. A higher sonotrode position within the hot top position leads to a slightly raised sump profile, with no elongated grains at the centre of the billet compared with the sonotrode aligned with the graphite ring level.

Acknowledgements

Financial support from EPSRC (UK) under projects Future LiME Hub

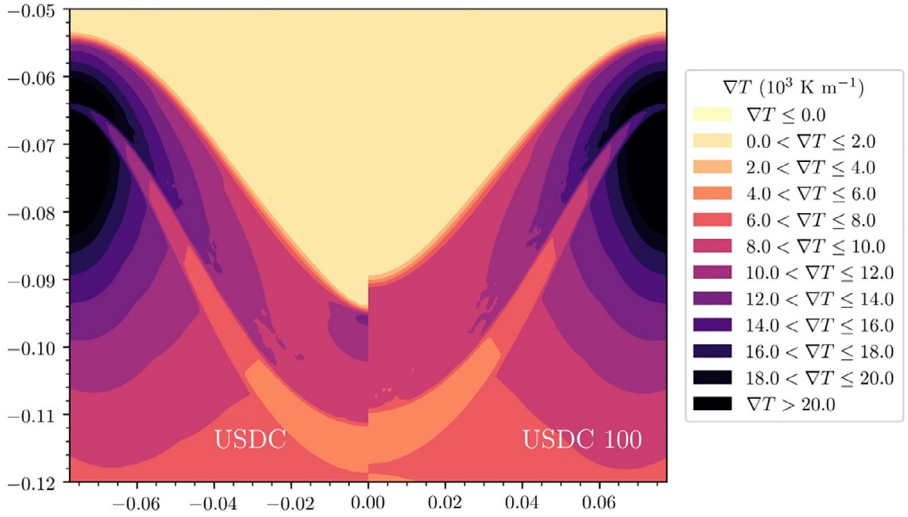

Fig. 12. Comparison between temperature gradients in USDC casting with the sonotrode (left) submerged to the level of the graphite ring and (right) positioned 100 mm above the graphite ring.

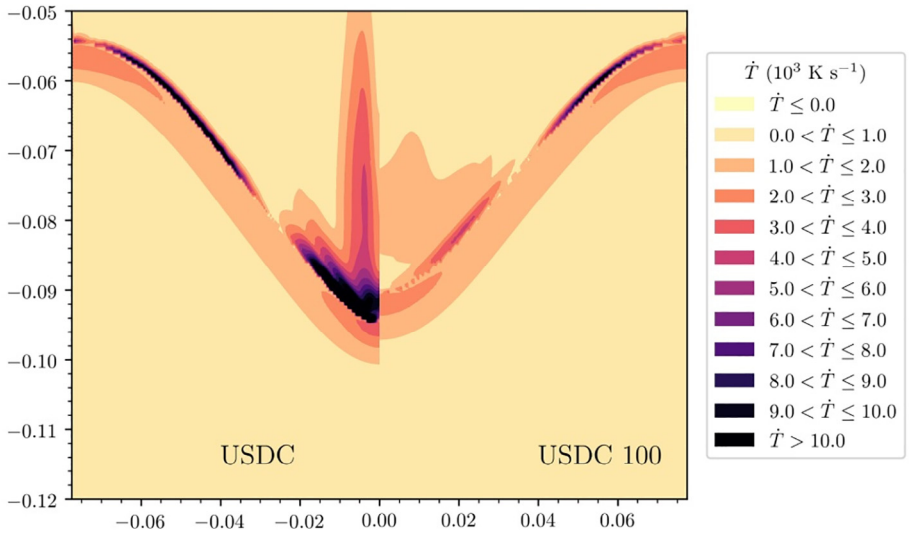

Fig. 13. Comparison between cooling rates in USDC casting with the sonotrode (left) submerged to the level of the graphite ring and (right) positioned 100 mm above the graphite ring.

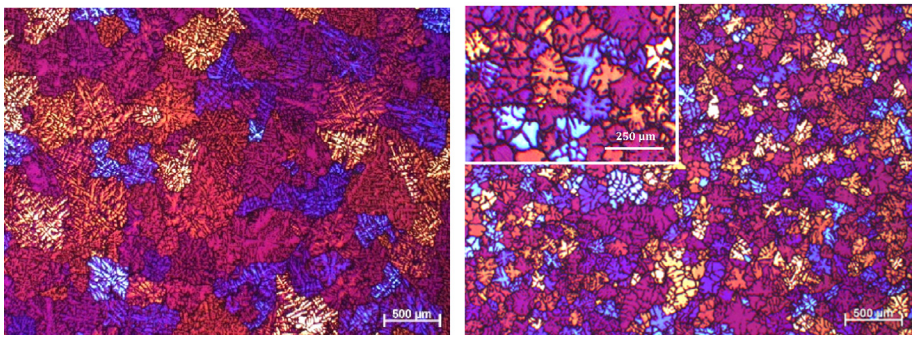

Fig. 14. Reference grain structure (without ultrasound) at half radius (left) and off-centre (right) of the billet.

(EP/N007638/1) and UltraMelt2 (EP/R011001/1, EP/R011044/1 and EP/R011095/1) is gratefully acknowledged.

Data availability statement

The processed data required to reproduce these findings are available to download from https://dx.doi.org/10.17633/rd.brunel.7610924.

Appendix A. Supplementary data

Supplementary data to this article can be found online at https://

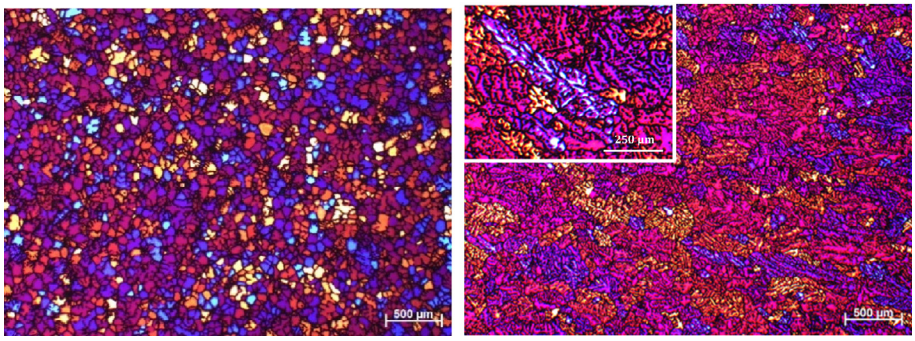

Fig. 15. Grain structure when the sonotrode is submerged to the level of the graphite ring at half radius (left) and off-centre (right) of the billet.

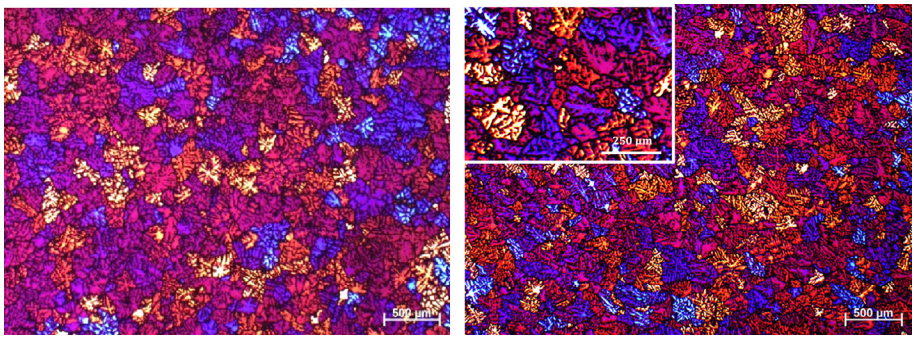

Fig. 16. Grain structure when the sonotrode is 100 mm above the graphite ring at half radius (left) and off-centre (right) of the billet.

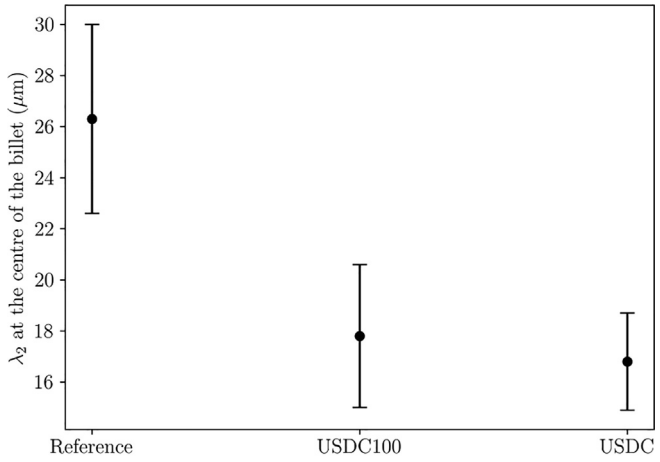

Fig. 17. Measured secondary dendrite arm spacing λ_2 at the centre of the billet.

doi.org/10.1016/j.ultsonch.2019.02.002.

References

[1] G.I. Eskin, D.G. Eskin, Ultrasonic treatment of light alloy melts, second ed., Taylor & Francis, CRC Press, Boca Raton, 2015.
[2] J. Ni, C. Beckermann, A volume-averaged two-phase model for transport phenomena during solidification, Metall. Trans. B 22 (1991) 349–361, https://doi.org/10.1007/BF02651234.
[3] W.D. Bennon, F.P. Incropera, A continuum model for momentum, heat and species transport in binary solid-liquid phase change systems—I. Model formulation, Int. J. Heat Mass Transf. 30 (1987) 2161–2170, https://doi.org/10.1016/0017-9310(87)90094-9.
[4] P.J. Prescott, F.P. Incropera, W.D. Bennon, Modeling of dendritic solidification systems: reassessment of the continuum momentum equation, Int. J. Heat Mass Transf. 34 (1991) 2351–2359, https://doi.org/10.1016/0017-9310(91)90060-R.
[5] C.J. Vreeman, M.J.M. Krane, F.P. Incropera, The effect of free-floating dendrites and convection on macrosegregation in direct chill cast aluminum alloys: Part I: model development, Int. J. Heat Mass Transf. 43 (2000) 677–686, https://doi.org/10.1016/S0017-9310(99)00174-X.
[6] C.J. Vreeman, J.D. Schloz, M.J.M. Krane, Direct chill casting of aluminum alloys: modeling and experiments on industrial scale ingots, J. Heat Transfer 124 (2002) 947–953, https://doi.org/10.1115/1.1482089.
[7] K. Pericleous, G. Djambazov, M. Ward, L. Yuan, P.D. Lee, A multiscale 3D model of the vacuum arc remelting process, Metall. Mater. Trans. A. 44 (2013) 5365–5376, https://doi.org/10.1007/s11661-013-1680-4.
[8] L. Heyvaert, M. Bedel, M. Založnik, H. Combeau, Modeling of the coupling of microstructure and macrosegregation in a direct chill cast Al-Cu billet, Metall. Mater. Transa. A. 48 (2017) 4713–4734, https://doi.org/10.1007/s11661-017-4238-z.
[9] K.O. Tveito, A. Pakanati, M. M'Hamdi, H. Combeau, M. Založnik, A simplified three-phase model of equiaxed solidification for the prediction of microstructure and macrosegregation in castings, Metall. Mater. Trans. A. (2018), https://doi.org/10.1007/s11661-018-4632-1.
[10] L.V. Wijngaarden, On the equations of motion for mixtures of liquid and gas bubbles, J. Fluid Mech. 33 (1968) 465, https://doi.org/10.1017/S002211206800145X.
[11] R.E. Caflisch, M.J. Miksis, G.C. Papanicolaou, L. Ting, Effective equations for wave propagation in bubbly liquids, J. Fluid Mech. 153 (1985) 259, https://doi.org/10.1017/S0022112085001252.
[12] L.L. Foldy, The multiple scattering of waves. I. general theory of isotropic scattering by randomly distributed scatterers, Phys. Rev. 67 (1945) 107–119, https://doi.org/10.1103/PhysRev.67.107.
[13] G.S.B. Lebon, I. Tzanakis, K. Pericleous, D. Eskin, Experimental and numerical investigation of acoustic pressures in different liquids, Ultrason. Sonochem. 42 (2018) 411–421, https://doi.org/10.1016/j.ultsonch.2017.12.002.
[14] K.W. Commander, A. Prosperetti, Linear pressure waves in bubbly liquids: comparison between theory and experiments, J. Acous. Soc. Am. 85 (1989) 732–746, https://doi.org/10.1121/1.397599.
[15] O. Louisnard, A simple model of ultrasound propagation in a cavitating liquid. Part I: theory, nonlinear attenuation and traveling wave generation, Ultrason. Sonochem. 19 (2012) 56–65, https://doi.org/10.1016/j.ultsonch.2011.06.007.
[16] R. Jamshidi, G. Brenner, Dissipation of ultrasonic wave propagation in bubbly liquids considering the effect of compressibility to the first order of acoustical Mach number, Ultrasonics 53 (2013) 842–848, https://doi.org/10.1016/j.ultras.2012.12.004.
[17] H. Dogan, V. Popov, Numerical simulation of the nonlinear ultrasonic pressure wave propagation in a cavitating bubbly liquid inside a sonochemical reactor, Ultrason. Sonochem. 30 (2016) 87–97, https://doi.org/10.1016/j.ultsonch.2015.11.011.
[18] F.J. Trujillo, A strict formulation of a nonlinear Helmholtz equation for the propagation of sound in bubbly liquids. Part I: theory and validation at low acoustic pressure amplitudes, Ultrason. Sonochem. 47 (2018) 75–98, https://doi.org/10.1016/j.ultsonch.2018.04.014.
[19] O. Louisnard, A viable method to predict acoustic streaming in presence of cavitation, Ultrason. Sonochem. 35 (2017) 518–524, https://doi.org/10.1016/j.ultsonch.2016.09.013.
[20] G.S.B. Lebon, I. Tzanakis, K. Pericleous, D. Eskin, P.S. Grant, Ultrasonic liquid metal processing: the essential role of cavitation bubbles in controlling acoustic streaming, Ultrason. Sonochem. (2019), https://doi.org/10.1016/j.ultsonch.2019.

01.021.
[21] G. Salloum-Abou-Jaoude, D.G. Eskin, G.S.B. Lebon, C. Barbatti, P. Jarry, M. Jarrett, Altering the microstructure morphology by ultrasound melt processing during 6XXX aluminium DC-casting, in: D. Eskin, K. Pericleous (Eds.), Light Metals 2019, 2019: p. Accepted.
[22] Y.A. Gadi Man, F.J. Trujillo, A new pressure formulation for gas-compressibility dampening in bubble dynamics models, Ultrason. Sonochem. 32 (2016) 247–257, https://doi.org/10.1016/j.ultsonch.2016.03.013.
[23] J.J. Jasper, The surface tension of pure liquid compounds, J. Phys. Chem. Ref. Data 1 (1972) 841–1010, https://doi.org/10.1063/1.3253106.
[24] W.W. Xu, I. Tzanakis, P. Srirangam, W.U. Mirihanage, D.G. Eskin, A.J. Bodey, P.D. Lee, Synchrotron quantification of ultrasound cavitation and bubble dynamics in Al–10Cu melts, Ultrason. Sonochem. 31 (2016) 355–361, https://doi.org/10.1016/j.ultsonch.2016.01.017.
[25] R. Toegel, B. Gompf, R. Pecha, D. Lohse, Does water vapor prevent upscaling sonoluminescence? Phys. Rev. Lett. 85 (2000) 3165–3168, https://doi.org/10.1103/PhysRevLett. 85.3165.
[26] V.R. Voller, C. Prakash, A fixed grid numerical modelling methodology for convection-diffusion mushy region phase-change problems, Int. J. Heat Mass Transf. 30 (1987) 1709–1719, https://doi.org/10.1016/0017-9310(87)90317-6.
[27] G.S.B. Lebon, I. Tzanakis, G. Djambazov, K. Pericleous, D.G. Eskin, Numerical modelling of ultrasonic waves in a bubbly Newtonian liquid using a high-order acoustic cavitation model, Ultrason. Sonochem. 37 (2017) 660–668, https://doi.org/10.1016/j.ultsonch.2017.02.031.
[28] D.M. Stefanescu, Science and engineering of casting solidification, second ed., Springer, New York, NY, 2009.
[29] F.R. Menter, M. Kuntz, R. Langtry, Ten Years of Industrial Experience with the SST Turbulence Model, in: Turbulence, Heat and Mass Transfer 4, Begell House, Antalya, Turkey, 2003: pp. 625–632.
[30] J.M. Reese, Characterization of the flow in the molten metal sump during direct chill aluminum casting, Metall. Mater. Trans. B. 28 (1997) 491–499, https://doi.org/10.1007/s11663-997-0116-1.
[31] J.A.J. Robinson, A.W.D. Hills, A.T. Dinsdale, R.F. Brooks, L.A. Chapman, B. Roebuck, P.N. Quested, Prediction of properties of steels relevant to process simulation, European Conference on Thermophysical Properties, 2005, p. 73.
[32] ProCAST, ESI Group, 2016.
[33] H.G. Weller, OpenFOAM, OpenCFD Ltd (ESI Group), 2018.
[34] G.F. Hewitt, Boiling, in: W.M. Rohsenow, J.P. Hartnett, Y.I. Cho (Eds.), Handbook of Heat Transfer, third ed., McGraw-Hill, New York, 1998, p. 46.
[35] F.R. Menter, T. Esch, Elements of industrial heat transfer predictions, 16th Brazilian Congress of Mechanical Engineering (COBEM), (2001).
[36] A.R. Baserinia, H. Ng, D.C. Weckman, M.A. Wells, S. Barker, M. Gallerneault, A simple model of the mold boundary condition in direct-chill (DC) casting of aluminum alloys, Metall. Mater. Trans. B. 43 (2012) 887–901, https://doi.org/10.1007/s11663-012-9658-y.
[37] I. Tzanakis, M. Hodnett, G.S.B. Lebon, N. Dezhkunov, D.G. Eskin, Calibration and performance assessment of an innovative high-temperature cavitometer, Sens. Actuators, A 240 (2016) 57–69, https://doi.org/10.1016/j.sna.2016.01.024.
[38] E. Jones, E. Oliphant, P. Peterson, others, SciPy: Open Source Scientific Tools for Python, 2018. https://www.scipy.org.
[39] L. Petzold, Automatic selection of methods for solving stiff and nonstiff systems of ordinary differential equations, SIAM J. Sci. Stat. Comput. 4 (1983) 136–148, https://doi.org/10.1137/0904010.
[40] I. Tzanakis, G.S.B. Lebon, D.G. Eskin, K. Pericleous, Investigation of the factors influencing cavitation intensity during the ultrasonic treatment of molten aluminium, Mater. Des. 90 (2016) 979–983, https://doi.org/10.1016/j.matdes.2015.11.010.
[41] I. Tzanakis, G.S.B. Lebon, D.G. Eskin, K.A. Pericleous, Characterizing the cavitation development and acoustic spectrum in various liquids, Ultrason. Sonochem. 34 (2017) 651–662, https://doi.org/10.1016/j.ultsonch.2016.06.034.
[42] J.A. Dantzig, M. Rappaz, Solidification, first ed., EPFL Press, Lausanne, 2009.
[43] W. Kurz, D.J. Fisher, Fundamentals of Solidification, fourth rev. ed. Trans Tech Publications, Uetikon-Zuerich, Switzerland; Enfield, N.H, 1998.
[44] G. Reinhart, H. Nguyen-Thi, N. Mangelinck-Noël, B. Billia, T. Schenk, J. Baruchel, CET during the solidification of refined Al-3.5wt%Ni alloys and characterization of the subsequent grain structure, IOP Conference Series, Mater. Sci. Eng. 27 (2012) 012011, , https://doi.org/10.1088/1757-899X/27/1/012011.